

# **Supplementary Material**

## **S1 Related data**

### **S1.1 Flood Occurrences**

Our study reconstructs paleoflood frequencies in the Hasli-Aare catchment, focusing on the Late Holocene period, using environmental proxies from delta plain sediments (Fig. 1, main text). These reconstructions were calibrated against historical data from textual sources, covering the last 520 years (Hilker et al., 2009; Schulte et al., 2015), and instrumental data starting from 1908 CE (Swiss Federal Research Institute WSL). To derive these proxies, we followed several analytical steps: We plotted individual chemical elements against lithology, grain-size, total organic carbon (TOC), and depth of the sediment samples; Titanium (Ti) ratios were used due to the element's conservative nature during transport and weathering (Kylander et al., 2011); A factor analysis was conducted to examine the variability in the geochemical data (see Fig. 1 main text, Flood\_F1); Zirconium (Zr)/Ti ratios were compared with grain-size fractions and flood layers, both at macro- and microscopic levels, to produce grain-size flood proxies. After 1920 CE, the sensitivity of these proxies decreased due to human-induced changes in floodplain deposition caused by channel corrections and flood protection measures.

### **S1.2 Climate Variables**

We analysed the interannual atmospheric variability of summer climate, using sea level pressure (SLP) anomalies from paleoclimate simulations. These simulations were validated against observed and reconstructed atmospheric data, including SLP grids from the Twentieth Century Reanalysis Project (Compo et al., 2011) and the EMULATE project (Luterbacher et al., 2002; Ansell et al., 2006). Simulations from the CESM-LME (Otto-Bliesner et al., 2016), incorporating full-forcing experiments (greenhouse gases, volcanic, solar radiation, and orbital changes) were examined over the period 1300–1849 CE (Pre-industrial) and 1850–2005 CE (Industrial) (Table S1).

This approach enables a comprehensive investigation of the period from 1300 to 2005, allowing us to examine how different forcings interact with key climatic variables. To assess their collective influence on the climate system, we derived a composite EOF (EOF1, Fig. S1) by integrating all forcings simultaneously. Furthermore, major modes of climate variability in high summer (July and August months) in the North Atlantic region are shown in Fig. S2 (adapted from Barnston and Livezey, 1987).

Observed and reconstructed summer sea level pressure (SLP) anomalies for July-August reveals a dominant spatial pattern characterized by positive anomalies over the Scandinavian Peninsula and the British Isles, alongside subtle low-pressure anomalies over the Mediterranean region (Peña et al., 2015). This pattern representing the principal mode of summer atmospheric variability, known as the Summer North Atlantic Oscillation (SNAO) (Fig. S1, Folland et al., 2009), and differs from the winter NAO by exhibiting a distinct northwest–southeast pressure gradient.

35  
36

**Table S1. Glossary.** All variables entered the causal analysis (using bnlearn in R) are defined below; except for the Flood Layers, which is illustrated in Fig. 1 of the main text.

| VARIABLE     | DESCRIPTION   | SOURCE  |
|--------------|---|---|
| Flood_F1     | First factor scores from factor analysis of sediment geochemistry (Hasli delta).  | Schulte et al., 2015 (see Fig. 1, Main Text)        |
| Flood Layers | Coarse-grained flood layers in Hasli delta sediments  | Schulte et al., 2015 (Fig. 1, Main Text)            |
| EOF1         | Principal EOF extracted from PCA in S-mode for industrial and pre-industrial period from SLP grids taken from CSEM-LME represented by the ensemble mean of full-forcing experiment based on internal variability captured by 13 full-forcing runs | Peña et al., 2015; also Fig. 1, Main Text           |
| TSI          | Total Solar Irradiance (reconstruction).  | Steinhilber et al., 2009                            |
| Pamj_Alps    | Alpine Spring precipitation (tree rings reconstructions).   | Büntgen et al., 2006, 2011                          |
| NH_Tja       | Northern Hemisphere July–August temperature (CESM-LME ensemble mean).   | Peña & Schulte, 2020                                |
| Tjja_Alps    | Alpine Summer temperature (tree-ring reconstructions).  | Büntgen et al., 2006, 2011, see Fig. 1 of Main Text |
| NH_Volcanic  | Northern Hemisphere stratospheric sulphate burden (Tg).   | Gao et al., 2008                                    |
| SNAO         | Summer North Atlantic Oscillation index (first PCA of summer SLP anomalies).  | Adapted from Barnston and Livezey (1987)            |
| EA           | East Atlantic pattern (second PCA of summer SLP anomalies).   |   |
| EATL.WRUS    | East Atlantic/Western Russia pattern (third PCA of summer SLP anomalies).   |   |
| AL           | Atlantic Low pattern (fourth PCA of summer SLP anomalies).  |   |
| OM           | Omega pattern (fifth PCA of summer SLP anomalies).  |   |
| AH           | Atlantic High pattern (sixth PCA of summer SLP anomalies).  |   |

37  
38

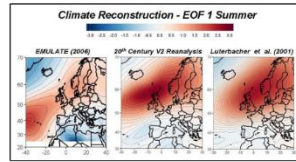
**Table S2.** Description of SLP grids and time series used herein.  
\* SNAO considering LUT and 20CR to complete the dataset for 1800–2005 (Details: Peña et al., 2015).

| Name                    | Acronym | Data     | Author Data       | Author    | Type          | Period         | Start | End  |
|-------------------------|---------|----------|-------------------|-----------|---------------|----------------|-------|------|
| Reconstructed Folland   | FOLr    | Time     | Folland 2009      | Folland   | Reconstructed | Only           | 1850  | 2005 |
| Observed Folland        | FOLo    | Time     | Folland 2009      | Folland   | Observed      | Pre+Industrial | 1706  | 1976 |
| EMULATE                 | EMU     | SLP grid | Jones 2006        | Peña 2020 | Reconstructed | Only           | 1850  | 2005 |
| SNAO*                   | SNAO    | Time     | Peña 2015         | Peña 2015 | Obs +         | Pre+Industrial | 1800  | 2005 |
| 20th century reanalysis | 20CR    | SLP grid | Compo et al. 2011 | Peña 2020 | Observed      | Only           | 1850  | 2005 |
| Luterbacher             | LUT     | SLP grid | Luterbacher 2002  | Peña 2015 | Reconstructed | Pre+Industrial | 1659  | 1999 |
| Last Millennium         | CESM-   | SLP grid | Otto-Bliesner     | Peña 2020 | Simulated     | Pre+Industrial | 1300  | 2005 |

**SNAO** → Dominant mode of climate variability in North Atlantic during July-August months

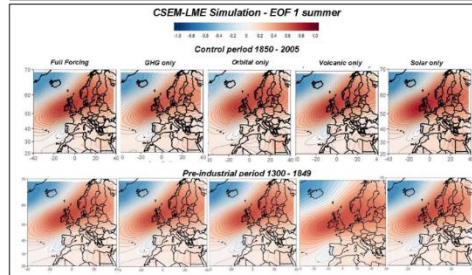
EOF 1 of SLP corrected anomalies over the North-Atlantic European sector (30W-30E:30N-70N)

A)



B)

CSEM-LME simulation EOF 1 Scores for SNAO.  
Industrial Period: 1850-2005 (up) Pre-Industrial Period: 1300-1849 (down)  
Ensemble Mean of Full Forcing and Radiative Forcing



C)

CSEM-LME simulation EOF 1 Scores for SNAO.  
1300-1849: Left panel. 1850-2005: Right panel. Dark grey lines: composite of all runs

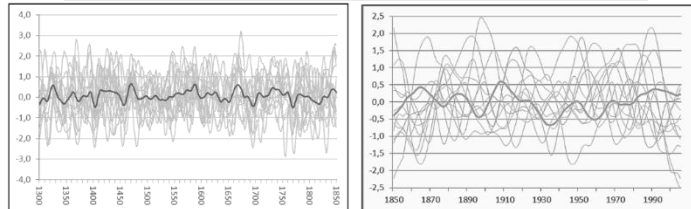
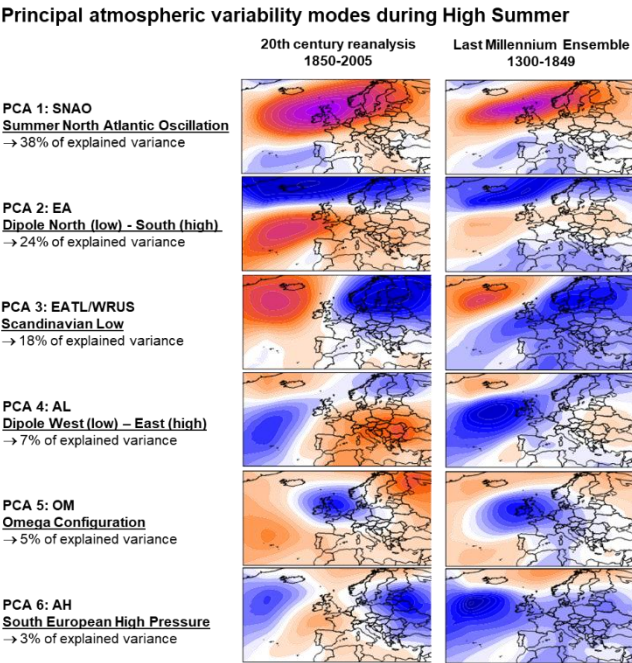
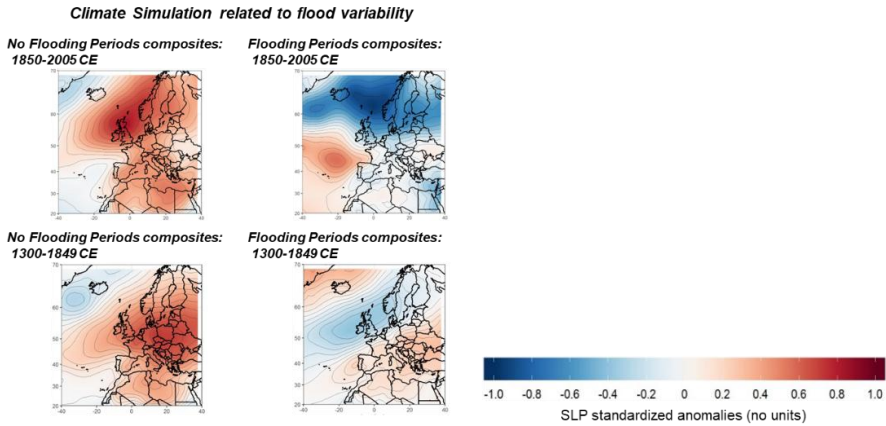


**Figure S1.** A) Interannual pattern of the atmospheric variability based on principal EOF extracted from PCA in S-mode, using the covariance matrix of corrected anomalies of SLP for July and August. B) Reconstructed pattern for the industrial period (1850-2005 CE) from SLP grids taken from EMULATE project, 20CR and LUT. The maps are the mean ensemble of 13 full forcing runs, and the ensemble mean of single forcing runs. C) Simulated pattern for industrial and pre-industrial period from SLP grids taken from CSEM-LME represented by the ensemble mean of full-forcing experiment for the principal EOF pattern (black line), based on internal variability captured by 13 full-forcing runs (grey lines).



48

49 **Figure S2.** Overview of the principal atmospheric variability modes during High Summer (July and August  
50 Months). The identification of Northern Hemisphere teleconnection patterns and indices is achieved using the  
51 Rotated Principal Component Analysis (RPCA) method, as described by Barnston and Livezey (1987). RPCA is  
52 particularly effective in isolating the dominant teleconnection patterns across High Summer, enabling the  
53 construction of time series that represent the temporal evolution of these patterns. For the purposes of this study, the  
54 RPCA technique is applied to monthly mean standardized SLP anomalies. These anomalies were derived from the  
55 20CR and CESM-LME within the analysis domain spanning 30°N to 70°N and -40°W to 40°E, covering the period  
56 1300-2005. The anomalies were standardized relative to the monthly means and standard deviations of the 1850-1900  
57 reference period, ensuring comparability across time and consistency with climatological norms.



58

59 **Figure S3.** Climate Simulation related to flood variability computed from 13 full-forcing simulations in the CSEM-  
60 LME. Left panel: No-flood periods SLP anomaly composites for the Industrial (top) and Pre-Industrial (bottom).

61 **References**

62 Ansell, T. J., Folland, C. K. & Alexander, L. V.: Reconstruction of daily mean sea level pressure over the  
63 European-North Atlantic region for the period 1850–2003. *J. Clim.* **19**, 2717–2742,  
64 <https://doi.org/10.1175/JCLI3775.1>, 2006.

- Barnston, A. G. & Livezey, R. E.: Classification, seasonality, and forecasting of low-frequency atmospheric circulation patterns. *Mon. Weather Rev.* **115**, 1083–1126, [https://doi.org/10.1175/1520-0493\(1987\)115<1083:CSAPOL>2.0.CO;2](https://doi.org/10.1175/1520-0493(1987)115<1083:CSAPOL>2.0.CO;2), 1987.
- Büntgen, U., Frank, D. C., Nievergelt, D. & Esper, J.: Summer Temperature Variations in the European Alps, a.d.755–2004. *J. Clim.* **19**, <https://doi.org/10.1175/JCLI3917.1>, 2006.
- Büntgen, U. et al.: 2500 years of European climate variability and human susceptibility. *Science* **331**, 578–582, <https://doi.org/10.1126/science.1197175>, 2011.
- Büntgen, U. et al. Prominent role of volcanism in Common Era climate variability and human history. *Dendrochronologia* **64**, 125757, <https://doi.org/10.1016/j.dendro.2020.125757>, 2020.
- Compo, G.P., Whitaker, J.S., Sardeshmukh, P.D., Matsui, N., Allan, R.J., Yin, X., Gleason, B.E., Vose, R.S., Rutledge, G., Bessemoulin, P., Brönnimann, S., Brunet, M., Crouthamel, R.I., Grant, A.N., Groisman, P.Y., Jones, P.D., Kruk, M.C., Kruger, A.C., Marshall, G.J., Maugeri, M., Mok, H.Y., Nordli, Ø., Ross, T.F., Trigo, R.M., Wang, X.L., Woodruff, S.D. and Worley, S.J.: The Twentieth Century Reanalysis Project. *Q.J.R. Meteorol. Soc.*, 137: 1–28. <https://doi.org/10.1002/qj.776>, 2011.
- Gao, C., Robock, A. & Ammann, C.: Volcanic forcing of climate over the past 1500 years: An improved ice-core-based index for climate models. *J. Geophys. Res.* **113**, D23111, <https://doi.org/10.1029/2008JD010239>, 2008.
- Hilker, N., Badoux, A. & Hegg, C. The Swiss flood and landslide damage database 1972–2007. *Nat. Hazards Earth Syst. Sci.* **9**, 913–925, <https://doi.org/10.5194/nhess-9-913-2009>, 2009.
- Hirschi, M., Seneviratne, S. I. & Schär, C. Seasonal variations in terrestrial water storage—Modelling and observations. *Geophys. Res. Lett.* **33**, L08404 (2006).
- Luterbacher, J., Xoplaki, E., Dietrich, D., Jones, P.D., Davies, T.D., Portis, D., Gonzalez-Rouco, J.F., von Storch, H., Gyalistras, D., Casty, C. and Wanner, H.: Extending North Atlantic oscillation reconstructions back to 1500. *Atmosph. Sci. Lett.*, 2: 114–124, <https://doi.org/10.1006/asle.2002.0047>, 2001.
- Otto-Bliesner, B. L., Brady, E. C., Fasullo, J., Jahn, A., Landrum, L., Stevenson, S., Rosenbloom, N., Mai, A., & Strand, G.: Climate Variability and Change since 850 CE: An Ensemble Approach with the Community Earth System Model. *Bulletin of the American Meteorological Society*, 97(5), 735–754. <https://doi.org/10.1175/BAMS-D-14-00233.1>, 2016.
- Peña, J. C., Schulte, L., Badoux, A., Barriendos, M. & Barrera-Escoda, A.: Influence of solar forcing, climate variability and modes of low-frequency atmospheric variability on summer floods in Switzerland. *Hydrol. Earth Syst. Sci.* **19**, 3807–3827, <https://doi.org/10.5194/hess-19-3807-2015>, 2015.
- Peña, J. C. & Schulte, L.: Simulated and reconstructed atmospheric variability and their relation with large pre-industrial summer floods in the Hasli-Aare catchment (Swiss Alps) since 1300 CE. *Glob. Planet. Change* **184**, 103052, <https://doi.org/10.1016/j.gloplacha.2019.103052>, 2020.
- Schulte, L., Peña, J. C., Carvalho, F., Schmidt, T., Julià, R., Llorca, J., and Veit, H.: A 2600-year history of floods in the Bernese Alps, Switzerland: frequencies, mechanisms and climate forcing, *Hydrol. Earth Syst. Sci.*, 19, 3047–3072, <https://doi.org/10.5194/hess-19-3047-2015>, 2015.
- Steinhilber, F., Beer, J. & Fröhlich, C.: Total solar irradiance during the Holocene. *Geophys. Res. Lett.* **36**, L19704 (2009). <https://doi.org/10.1029/2009GL040142>, 2009.
- Tveito, O. E. et al. *Nordic temperature maps* Report No. 09/00 (Norwegian Meteorological Institute, 2000).

## S2 Complementary Causality test (Granger Causality)

### S2.1 Methodology

The Granger causality test (Granger, 1969) is a statistical hypothesis test for time series. It checks if past values of one variable help predict another. Granger causality does not prove true causation, only temporal precedence (i.e., X leads Y in time). It assumes linearity and stationarity, which may not hold perfectly in climate data (e.g., volcanic responses can be nonlinear).

The test requires choosing a lag order (number of past observations). Too few lags can miss relationships; too many can reduce power. Characteristic lag-times for our variables are shown in Table S3 (cited from literature).

**Table S3.** Typical lag-times for external/internal forcings (from literature)

| Variable                              | Lag (years) | Source                 |
|---------------------------------------|-------------|------------------------|
| Solar Activity (TSI)                  | 5 - 10      | Rind et., 1999         |
| Volcanic activity (NH_Volcanic)       | > 10        | Sigl et al., 2015      |
| Summer atmospheric circulation (EOF1) | 0.5 - 2     | Tabari & Willems, 2018 |

Notes: Rind et al. (1999) reported that global surface temperatures lag solar fluctuations by up to ~10 years, with ocean regions showing smaller phase lags. Major volcanic eruptions can cool climate for several years (Sigl et al., 2015). Tabari & Willems (2018) describe how summer circulation patterns over the Mediterranean influence summer precipitation and carry impacts into subsequent seasons.

Granger testing provides a necessary (but not sufficient) condition for causality: if X Granger-causes Y (p-values below threshold), X precedes and helps predict Y. In contrast, the PC algorithm finds conditional independencies without explicit lags. We use Granger results to reinforce or question causal links from PC-stable. We follow conventional p-value interpretation:

- $p < 0.05$ : Strong evidence X Granger-causes Y (predictor significantly improves the forecast).
- $0.05 \leq p \leq 0.10$ : Weak/moderate evidence of Granger causality (marginal improvement).
- $p > 0.10$ : No significant Granger causality detected.

### S2.2 Results

Using the characteristic lags above, our Granger analysis identifies several significant or marginal causal relationships (Table 4 in main text), reveals several statistically significant and moderately significant temporal relationships between the investigated variables. These findings offer a complementary perspective to the structural relationships identified by the PC-stable algorithm.

#### S2.2.1 Significant Granger Causal Relationships ( $p < 0.05$ )

The following pairs of variables exhibit statistically significant Granger causality, indicating that past values of the first variable provide useful information for predicting future values of the second variable:

- **TSI → Pamj\_Alps ( $p = 0.006594$ ):** This result suggests a statistically significant influence of Total Solar Irradiance (TSI) on the precipitation index for the Pamir and the Alps (Pamj\_Alps) over time. The analysis indicates that variations in solar activity precede and are associated with changes in regional precipitation patterns. Notably, this causal direction is also present in the Pre-

Industrial Directed Acyclic Graph (DAG) with tiered structures, reinforcing a potential solar-driven hydroclimatic signal in these Alpine regions.

- **NH\_Volcanic → Tjja\_Alps ( $p < 0.001$ ):** A strong and highly significant Granger causal relationship is found between Northern Hemisphere volcanic activity (NH\_Volcanic) and summer temperatures in the Bernese Alps (Tjja\_Alps). This indicates that past volcanic eruptions are a significant predictor of subsequent temperature variations in the region, consistent with the established understanding of volcanic cooling effects. This causal link is also identified in the Pre-Industrial DAG with tiered structures.
- **EOF1 → Tjja\_Alps ( $p = 0.033275$ ):** The principal mode of atmospheric variability (EOF1) shows a statistically significant Granger causal influence on summer temperatures in the Bernese Alps (Tjja\_Alps). This suggests that large-scale atmospheric circulation patterns play a role in shaping regional temperature variability over time. This relationship is also observed in the Pre-Industrial DAG with tiered structures.
- **NH\_Tja → Tjja\_Alps ( $p = 0.025266$ ):** A statistically significant Granger causal relationship is detected between the Northern Hemisphere average temperature (NH\_Tja) and summer temperatures in the Bernese Alps (Tjja\_Alps). This finding suggests a potential lagged influence of hemispheric-scale temperature changes on regional Alpine temperatures. This causal direction is also present in the Pre-Industrial DAG with tiered structures.
- **NH\_Tja → Pamj\_Alps ( $p = 0.000079$ ):** A highly significant Granger causal link is found between Northern Hemisphere average temperature (NH\_Tja) and the precipitation index for the Pamir and the Alps (Pamj\_Alps). This suggests a potential lagged impact of hemispheric temperature changes on regional precipitation patterns in these Alpine regions. This causal relationship is also present in the Pre-Industrial DAG with tiered structures.
- **Pamj\_Alps → Flood\_F1 ( $p = 0.000079$ ):** A highly significant Granger causal relationship is observed between the precipitation index for the Pamir and the Alps (Pamj\_Alps) and the flood frequency factor (Flood\_F1). This indicates that long-term changes in precipitation significantly precede and contribute to variations in flood occurrence. Interestingly, this specific causal relationship is **not** present in the Pre-Industrial DAG with tiered structures at the selected confidence threshold.

### S2.2.2 Moderate Evidence of Granger Causality ( $0.05 < p \leq 0.1$ )

The following relationships exhibit moderate statistical significance, suggesting potential temporal influences that warrant consideration, although the evidence is less robust than the significant relationships:

- **TSI → EOF1 ( $p = 0.094418$ ):** This marginally significant result suggests a possible influence of solar variability on large-scale atmospheric circulation patterns (EOF1), although the statistical evidence is not strong. This causal relationship is present in the Unconstrained DAG.
- **NH\_Volcanic → NH\_Tja ( $p = 0.098691$ ):** A marginally significant Granger causal link is observed between Northern Hemisphere volcanic activity (NH\_Volcanic) and Northern Hemisphere average temperature (NH\_Tja), hinting at a potential feedback mechanism, though the evidence is weak. This causal relationship is **not** present in the Unconstrained DAG.

- **NH\_Volcanic → P.smooth.13.yr (p = 0.076843):** This marginally significant result suggests a potential lagged influence of Northern Hemisphere volcanic activity on the 13-year smoothed Alpine precipitation (P.smooth.13.yr), although the evidence is not strong. This causal relationship is **not** present in the Unconstrained DAG.
- **NH\_Volcanic → Flood\_F1 (p = 0.078823):** A marginally significant Granger causal relationship is found between Northern Hemisphere volcanic activity (NH\_Volcanic) and the flood frequency factor (Flood\_F1). This suggests a potential indirect influence of volcanic eruptions on flood variability, possibly mediated through changes in temperature and precipitation patterns. This causal relationship is **not** present in the Unconstrained DAG.
- **EOF1 → Pamj\_Alps (p = 0.078813):** This marginally significant result suggests a possible influence of large-scale atmospheric circulation patterns (EOF1) on the precipitation index for the Pamir and the Alps (Pamj\_Alps), although the evidence is not strong. This causal relationship is present in the Unconstrained DAG.
- **EOF1 → Flood\_F1 (p = 0.096750):** A marginally significant Granger causal relationship is observed between the principal mode of atmospheric variability (EOF1) and the flood frequency factor (Flood\_F1), suggesting a potential influence of large-scale atmospheric circulation on flood variability, though not strongly supported statistically. This causal relationship is **not** present in the Unconstrained DAG.
- **NH\_Tja → Flood\_F1 (p = 0.050422):** This marginally significant result suggests a possible lagged influence of Northern Hemisphere average temperature (NH\_Tja) on the flood frequency factor (Flood\_F1). Although the statistical evidence is moderate, this causal relationship is **not** present in the Pre-Industrial DAG with tiered structures.

## References

- Granger, C. W. J.: Investigating causal relations by econometric models and cross-spectral methods. *Econometrica*, 37(3), 424–438. <https://doi.org/10.2307/1912791>, 1969.
- Rind, D., Lean, J., Healy, R.: Simulated time-dependent climate response to solar radiative forcing since 1600. *Journal of Geophysical Research*, 104 (D2), 1973–1990, <https://doi.org/10.1029/1998JD200020>, 1999.
- Sigl, M., Winstrup, M., McConnell, J. R., Welten, K. C., Plunkett, G., Ludlow, F., Büntgen, U., Caffee, M. W., Chellman, N., Dahl-Jensen, D., Fischer, H., Kipfstuhl, S., Kostick, C., Maselli, O. J., Mekhaldi, F., Mulvaney, R., Muscheler, R., Pasteris, D. R., Pilcher, J. R., ... Woodruff, T. E.: Timing and climate forcing of volcanic eruptions for the past 2,500 years. *Nature*, 523(7562), 543–549, <https://doi.org/10.1038/NATURE14565>, 2015.
- Tabari, H., Willems, P. Lagged influence of Atlantic and Pacific climate patterns on European extreme precipitation. *Sci Rep* 8, 5748. <https://doi.org/10.1038/s41598-018-24069-9>, 2018.



### S3 PC-stable algorithm

We implemented a causal inference framework using the PC-stable algorithm (`pc.stable()`) available in the `bnlearn` package in R. This approach is based on constraint-based structure learning, relying on conditional independence tests to recover the causal graph structure from observational data. Unlike probabilistic or regression-based causal models, the PC-stable algorithm does not estimate causal effect sizes but instead identifies the skeleton of the causal network and orients edges using local conditional independencies.

To construct the causal network, we first standardized all input time series and ensured temporal alignment across datasets, spanning both pre-industrial and industrial periods. We applied the PC-stable algorithm with a conservative significance threshold ( $\alpha = 0.1$ ) to reduce false-positive edges. The conditional independence tests were based on partial correlation (Gaussian CI test), suitable for continuous, approximately Gaussian variables.

To assess the robustness of the inferred causal structure, we conducted 100 bootstrap resamplings of the original dataset. In each bootstrap iteration, we introduced random temporal perturbations (i.e., lagged noise and reordered blocks of data) to emulate realistic observational uncertainties and test the stability of causal directions under changing data conditions. Edges were retained in the final network only if they appeared in more than 80% of bootstrap replicates with consistent orientation.

We additionally performed cross-validation by splitting the dataset into two subsets: one corresponding to pre-industrial conditions and the other to the industrial era. This allowed us to test whether the inferred causal relations—particularly those between solar activity, SNAO, and hydrological extremes—were stable across distinct climatic and anthropogenic forcing regimes.

All analyses were conducted in R (v. 4.3.2) using the `bnlearn` and `lmtest` packages, with all scripts and data processing routines available via the project's open-access repository.

More specifically:

When using `pc.stable()` algorithm with the exact Student's t test (`test = cor`):

- The algorithm uses partial correlation tests.
- These tests assess whether two variables are conditionally independent given a conditioning set, based on the t-distribution derived from the partial correlation.
- It uses a t-statistic to compute a p-value for the null hypothesis that the partial correlation is zero (e.g. Kalisch & Bühlmann, 2007; Scutari, 2010).

Internally:

If  $X$  and  $Y$  are the two variables, and  $Z$  is the conditioning set, the test checks:

$$H_0 : \rho_{XY|Z} = 0$$

Then it computes a test statistic:

$$t = \rho \sqrt{\frac{n-|Z|-2}{1-\rho^2}} \quad \text{which follows a t-distribution with } n - |Z| - 2 \text{ degrees of freedom}$$

#### 1. Directionality in PC-Stable

- Directionality is inferred from collider structures, i.e., triples of nodes  $X \rightarrow Z \leftarrow Y$ , called *v-structures*.
- Once the skeleton is built (i.e., undirected edges after CI testing), directions are assigned based on specific rules, not based on probabilities or strength.

- The algorithm does not assign directionality based on causal strength but based on graph-theoretic rules that ensure acyclicity and consistency with observed conditional independencies.

## 2. Edge Strength

The edge strength is estimated via bootstrapping (with the function `boot.strength()` of `bnlearn` package), the strength is:

- The proportion of times an edge appears across bootstrap replicates.
- It's not a causal effect size or partial correlation coefficient.
- It reflects stability and confidence, not effect magnitude.

## References

- Kalisch, M., & Bühlmann, P.: Estimating high-dimensional directed acyclic graphs with the PC-algorithm. *Journal of Machine Learning Research*, 8, 613–636, <https://doi.org/10.48550/arXiv.math/0510436>, 2007.
- Scutari, M.: Learning Bayesian Networks with the `bnlearn` R Package. *Journal of Statistical Software*, 35(3), 1-22, <https://doi.org/10.18637/jss.v035.i03>, 2010.

**Table S4.** Strengths of paths (threshold significant strength = 0.58)

| PATH                             | STRENGHT |
|----------------------------------|----------|
| TSI -> Factor_1                  | 0,99     |
| TSI -> P.smooth.13.yr            | 1,00     |
| EOF1 -> T_Be                     | 1,00     |
| Factor_1 -> P.smooth.13.yr       | 1,00     |
| NH..Tg. -> T_Be                  | 1,00     |
| T.smooth.22.yr -> P.smooth.13.yr | 1,00     |
| T.smooth.22.yr -> T_Be           | 1,00     |

**Table S5.** Strengths of paths with domain constraints (threshold significant strengths = 0.41)

| PATH                             | STRENGHT |
|----------------------------------|----------|
| TSI -> EOF1                      | 1,00     |
| TSI -> flood_time                | 0,57     |
| TSI -> P.smooth.13.yr            | 1,00     |
| EOF1 -> flood_time               | 0,44     |
| EOF1 -> P.smooth.13.yr           | 0,77     |
| EOF1 -> T_Be                     | 1,00     |
| NH..Tg. -> T_Be                  | 1,00     |
| T.smooth.22.yr -> P.smooth.13.yr | 1,00     |
| T.smooth.22.yr -> T_Be           | 1,00     |

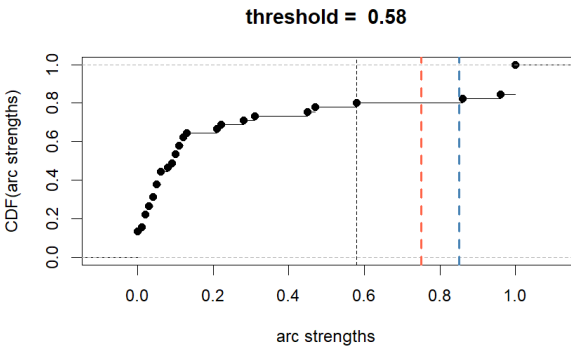
**Table S6.** Edge Stability Under Dating Uncertainty for Pre- industrial vs Industrial periods

| Edge from      | Edge to        | Industrial     |       |
|----------------|----------------|----------------|-------|
|                |                | Pre-Industrial | I     |
| TSI            | EOF1           | TRUE           | TRUE  |
| TSI            | P.smooth.13.yr | TRUE           | FALSE |
| TSI            | flood_time     | TRUE           | FALSE |
| TSI            | T_Be           | FALSE          | TRUE  |
| TSI            | EA             | FALSE          | TRUE  |
| EATL.WRUS      | EA             | TRUE           | FALSE |
| EOF1           | T_Be           | TRUE           | FALSE |
| EOF1           | P.smooth.13.yr | TRUE           | FALSE |
| EOF1           | T.smooth.22.yr | FALSE          | TRUE  |
| EOF1           | EA             | FALSE          | TRUE  |
| NH..Tg.        | T_Be           | TRUE           | TRUE  |
| SNAO           | EA             | TRUE           | TRUE  |
| T.smooth.22.yr | T_Be           | TRUE           | TRUE  |
| T.smooth.22.yr | P.smooth.13.yr | TRUE           | FALSE |
| T.smooth.22.yr | flood_time     | FALSE          | TRUE  |

270

271

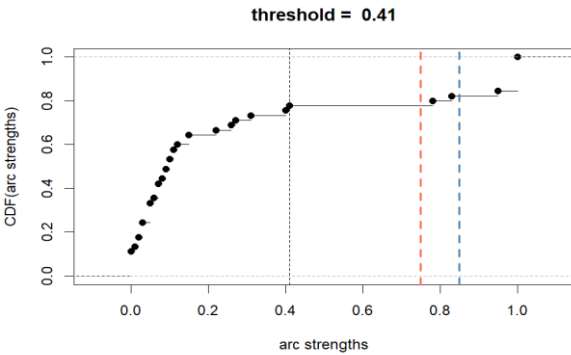
**Figure S4.** Strengths arcs of the DAG



272

273

**Figure S5.** Arc strengths of the DAG arcs with domain constraints



274

**Figure S6.** Constrained Pre-industrial Network Structure (edges with >41% confidence) Constrained Pre-industrial Network Structure (edges with >41% confidence).

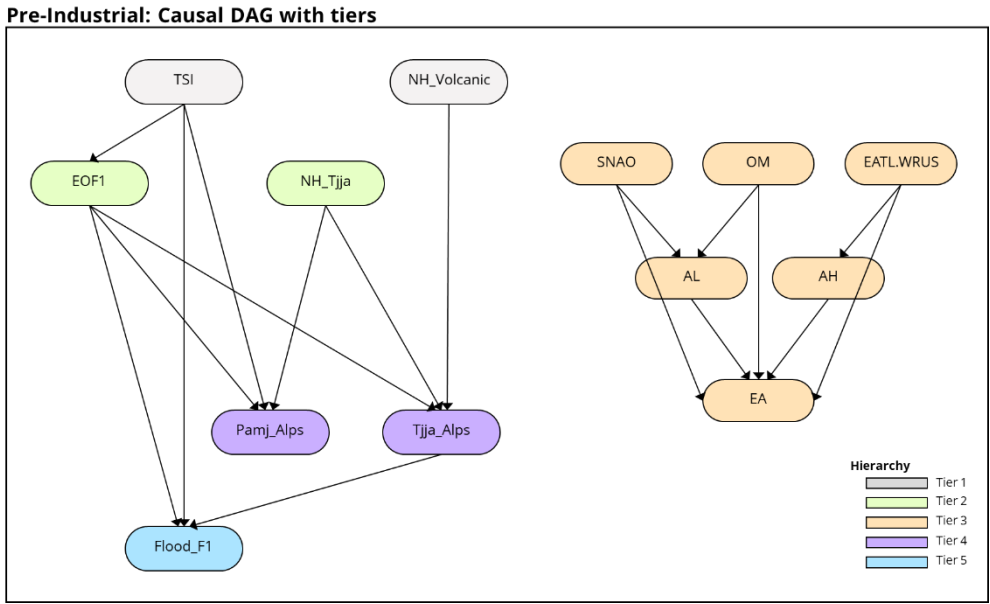


**Figure S7.** Bootstrapping of the n = 100 simulations of Out-of-sample log-likelihood

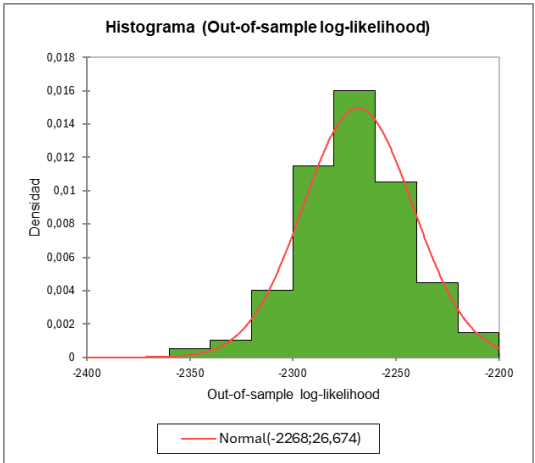


**Figure S8.** Arc strengths of the DAG arcs with domain constraints

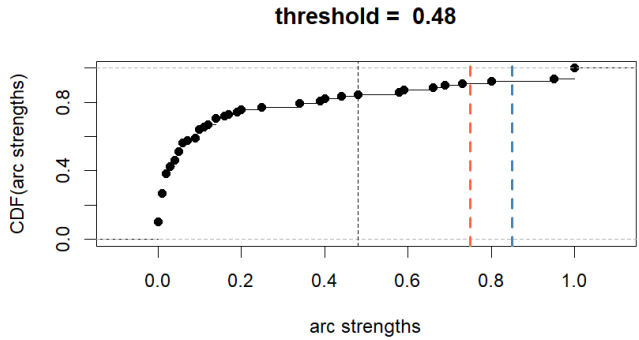


**Figure S9.** Constrained -industrial Network Structure (edges with > 48% confidence) with the strengths of the edges: cold colours (weak strengths) to warm colours (strong strengths).

